Direct Deposition of Anatase TiO_2 on Thermally Unstable Gold Nanobipyramid: Morphology-Conserved Plasmonic Nanohybrid for Combinational Photothermal and Photocatalytic Cancer Therapy

Dohyub Jang [a,b], Subin Yu [c], Kyungwha Chung [c], Jounghyun Yoo [b], Filipe Marques Mota [c], Jianfang Wang [d], Dong June Ahn [a,e,f], Sehoon Kim [b,f,], Dong Ha Kim [c,g,h,*]*

[a] Department of Biomicrosystem Technology, Korea University, Seoul 02792, Republic of Korea

[b] Center for Theragnosis, Korea Institute of Science and Technology, 5 Hwarang-ro 14-gil, Seongbuk-gu, Seoul 02792, Republic of Korea

[c] Department of Chemistry and Nano Science, Ewha Womans University, Seoul 03760, Republic of Korea

[d] Department of Physics, The Chinese University of Hong Kong, Shatin, Hong Kong SAR, China

[e] Department of Chemical and Biological Engineering, Korea University, Seoul 02841, Republic of Korea

[f] KU-KIST Graduate School of Converging Science and Technology, Korea University, Seoul 02841, Republic of Korea

[g] Basic Sciences Research Institute (Priority Research Institute), Ewha Womans University, 52,

Ewhayeodae-gil, Seodaemun-gu, Seoul 03760, Republic of Korea

[h] Nanobio·Energy Materials Center (National Research Facilities and Equipment Center), Ewha Womans University, 52, Ewhayeodae-gil, Seodaemun-gu, Seoul 03760, Republic of Korea

[*] Corresponding author.

E-mail addresses: dhkim@ewha.ac.kr (D. H. Kim), sehoonkim@kist.re.kr (S. Kim).

ABSTRACT

Deposition of crystalline titanium dioxide (TiO_2) on gold nanostructures has been considered as a promising strategy for near-infrared (NIR) light-activated photocatalysis. A typical route comprises pre-deposition of amorphous TiO_2 on the gold surface and ensuing crystallization by high-temperature annealing. Such condition, however, is not compatible with thermally unstable sharp-tipped gold nanostructures, causing structural disruption and plasmonic decline. Herein, we report a hybridization method excluding high-temperature annealing, i.e., direct deposition of anatase TiO_2 onto sharp-tipped gold nanobipyramid (Au NBP/a-TiO_2) with conserving their morphology without agglomeration via low-temperature hydrothermal reaction. In addition to keeping the plasmonic photothermal performance, Au NBP/a-TiO_2 exhibits enhanced photocatalytic generation of reactive oxygen species in response to the NIR excitation, evidencing the efficient injection of hot electrons from the Au NBP to the anatase shell. In vitro and in vivo studies revealed that the efficient photocatalytic/photothermal responses of Au NBP/a-TiO_2, along with dispersion stability in biological media and minimal toxicity, hold potential for synergistic photothermal and photodynamic therapy. We believe that the low-temperature synthetic method introduced here might offer a general way of deposition of crystalline TiO_2 on a variety of plasmonic nanostructures, broadening the spectrum of NIR-responsive photocatalytic hybrid nanostructures for biomedical applications.

KEYWORDS: gold nanobipyramid, heterojunction structure, photodynamic therapy, anatase titanium dioxide, near-infrared photocatalysis

1. Introduction

Inorganic nanomaterials have shown enormous potential for photocatalysis [1-4], where hierarchical hybrid structures are often employed to offer otherwise unachievable new properties and multifunctionalities [5-7]. For instance, semiconductor titanium dioxide (TiO_2) is hybridized with plasmonic noble metal nanostructures or upconversion nanoparticles to expand its UV-confined photocatalytic activity to the near-infrared (NIR) [5,8]. TiO_2 is a promising candidate of biocompatible inorganic photomedicine, and anatase phase has gathered distinct attraction owing to its better photocatalytic efficiency than other polymorphs [9,10]. However, its large band gap (3.2 eV) corresponding to the UV represents evident limitations in the *in vivo* applications because UV photons have limited tissue penetration and phototoxicity [11-13]. In this regard, many efforts have been made for spectral expansion of the TiO_2 photoactivity to the tissue-penetrating NIR [14], in particular by hybridization with a variety of anisotropic gold nanostructures that have broadly tunable localized surface plasmon resonance (LSPR) properties under the NIR light incidence [15,16].

As aforementioned, the hybridization with plasmonic nanostructures can redeem the spectral limit of TiO_2 by tuning the photoactivity to the NIR. From a chemical viewpoint, however, highly anisotropic gold nanostructures are intrinsically incompatible with anatase TiO_2 for hybridization because their thermal stability is generally too low to survive the harsh synthesis condition required for anatase crystallization (i.e., high-temperature annealing at above 200 °C) [17]. For instance, sharp-tipped gold nanobipyramid (Au NBP) that creates much stronger LSPR-enhanced electric field than blunt gold nanorods [18], likely undergoes partial melting during high-temperature crystallization of surface-deposited amorphous TiO_2 to anatase, to lose their tip sharpness and the initial LSPR properties thereby [19]. For this reason,

hybridization between Au NBP and TiO_2, reported in the literature, was attempted only with amorphous phase other than crystalline polymorphs [20-21]. Moreover, agglomeration of such hybrid colloids is inevitable during high-temperature anatase crystallization due to the occurrence of fusion between surface-deposited TiO_2, compromising the photocatalytic activity as well as colloidal stability for biomedical uses [19,22]. Therefore, deposition of anatase TiO_2 on the surface of sharp-tipped gold nanostructures while keeping the highly anisotropic morphology and colloidal stability intact, remains a big challenge.

In this study, we devised a novel synthetic strategy for hybridization of thermally unstable anisotropic gold nanostructures with anatase TiO_2, which utilizes the low-temperature hydrothermal reaction to allow direct crystalline deposition of anatase TiO_2 onto the gold surface without high-temperature annealing. Applying this method, we successfully developed unprecedented anatase TiO_2-decorated sharp-tipped Au NBP (Au NBP/a-TiO_2) with high photocatalytic activity and colloidal stability in water, being useful for NIR-responsive phototherapy of cancer. The attained nanoscopic hybridization facilitates NIR-responsive photocatalytic generation of reactive oxygen species (ROS) by following the proposed mechanism (**Scheme 1**), where highly energetic LSPR-derived hot electrons are generated on the Au-NBP surface by incident NIR light and then injected directly into the conduction band of the deposited anatase TiO_2 nanoclusters, to lead to the reduction of nearby oxygen to superoxide ($O_2^{\cdot -}$) and finally to hydroxyl radical ($\cdot OH$) [5]. Herein, we demonstrate that the shape-conserved sharp-tipped Au NBP core in the obtained nanohybrid (Au NBP/a-TiO_2) retains strong LSPR-induced electric field enhancement to show efficient anatase-coupled ROS generation as well as plasmonic photothermal heating under NIR excitation. With these NIR-responsive properties integrated into a single nanohybrid framework, Au NBP/a-TiO_2 was successfully applied to

combinational photodynamic/photothermal cancer therapy *in vivo*. Our work emphasizes the potential of our facile and mild synthetic approach for expanding the biomedical promise of hierarchical hybrid materials between thermally unstable plasmonic nanostructures and highly photocatalytic anatase TiO_2.

2. Materials and methods

2.1. Materials and instruments

2.1.1. Materials

Gold(III) chloride trihydrate ($HAuCl_4 \cdot 3H_2O$; ≥99.9% trace metals basis), trisodium citrate dihydrate, sodium borohydride ($NaBH_4$, 99%), hexadecyltrimethylammonium bromide (CTAB, ≥98%), silver nitrate ($AgNO_3$, ≥99.0%), ascorbic acid (AA), hexadecyltrimethylammonium chloride (CTAC, ≥98.0%), terephthalic acid (TA, 98%), hydrochloric acid (HCl, ACS reagent, 37%), glacial acetic acid (ACS reagent ≥99.7%), titanium(IV) isopropoxide (TTIP, ≥97%), tetraethyl orthosilicate (TEOS, ≥99.0%), and hydroethidine were all purchased from Sigma-Aldrich. Ammonia solution ($NH_3 \cdot H_2O$, 30%) was purchased from Daejung chemical. Hydrogen peroxide (H_2O_2, 30%) was purchased from Junsei Chemical Co. Ltd. Ethanol (EtOH, ACS reagent, absolute alcohol, ≥99.8%) was purchased from Fluka. The solvents were used without further purification.

2.1.2. Instruments

Transmission electron microscopy (TEM) was performed with a FEI Tecnai G2 F20 at 200 kV. Elemental analysis and mapping were carried out by energy dispersive X-ray spectroscopy (EDX) using a Talos F200X at 200 kV. UV-vis absorption and photoluminescence (PL) spectra were measured by an Agilent Cary300 UV−vis spectrophotometer and a Quanta master QM-40

spectrofluorometer, respectively. Powder X-ray diffraction patterns (XRD) were obtained by a D8 Advance (LynxEye). The 808 nm laser (Hi-Tech Optoelectronics Co. Ltd, 2 W/cm^2) was used as an excitation source to test photothermal and photodynamic effects.

2.2. Methods

2.2.1. Synthesis of Au NBP

Au NBP was synthesized by a seed-mediated method. The seed solution was synthesized by mixing trisodium citrate aqueous solution (0.01 M, 0.25 mL) and Gold (III) chloride trihydrate (0.01 M, 0.125 mL) in water (9.625 mL) with ice-cold NaBH4 aqueous solution (0.01 M, 0.15 mL) in a 50 mL of falcon tube. After mixing for 10 s, the solution was kept at room temperature for 2 h. The growth solution was prepared with sequential addition of Gold (III) chloride trihydrate solution (0.01 M, 2 mL), silver nitrate solution (0.01 M, 0.4 mL), hydrogen chloride solution (1 M, 0.8 mL), and ascorbic acid solution (0.1 M, 0.32 mL) into a CTAB solution (0.1 M, 40 mL). After solution color was disappeared, the seed solution (0.4 mL) was added to the growth solution, followed by gentle mixing for 10 s. The reaction solution was kept at ambient condition.

2.2.2. Purification of Au NBP

The as-grown Au NBP solution (40 mL) was centrifuged at 11,000 rpm for 20 min. After supernatant removal, CTAC solution (0.08 M, 20 mL) was added to the precipitation. Silver nitrate solution (0.01 M, 8 mL) and ascorbic acid solutions (0.1 M, 4 mL) were added to carry out Ag overgrowth. The resultant solution was kept at 60 °C for 4 h to obtain Au/Ag products. The bimetallic products were washed by centrifuge at 10,500 rpm for 20 min. The bimetallic product was redispersed in CTAB (0.1 M, 10 mL) and left overnight at room temperature without disturbing, during which the Au/Ag heteronanorods were aggregated and precipitated to

the bottom of falcon tube while the spherical nanoparticles remained in the CTAB solution. After removing the supernatant, the precipitate was redispersed in water (10 mL), ammonium solution (30 wt%, 0.4 mL) and hydrogen peroxide solution (6 wt%, 0.2 mL) were subsequently added four times with 1 h intervals to the resultant solution. The Ag segments were gradually etched in this process and silver chloride precipitate was generated on the bottom of the falcon tube. The supernatant was taken out and washed by centrifuge at 11,000 rpm for 20 min. Gold bipyramids were redispersed in a CTAB solution (0.01 M, 10 mL) for further use.

2.2.3. Synthesis of silica coated Au NBP

Au NBP was re-dispersed in CTAB solution (0.005 mM, 10 mL). Then, NaOH solution (0.1 M, 0.1 mL) was added, followed by adding TEOS:EtOH (2:8, 0.03 mL) solution three times every 30 min under vigorous stirring. After 2 h, silica coated Au NBP (Au NBP@SiO_2) was washed with DI water by centrifugation.

2.2.4. Synthesis of TiO_2-deposited Au NBP@SiO_2

Au NBP@SiO_2 was re-dispersed in EtOH:DI water (1 : 1, 10 mL). After addition of acetic acid (1 mL), EtOH-diluted TTIP (0.17 μL/mL, 2.5 mL) solution was added dropwise to the solution. The mixture was heated to 80 °C and kept at that temperature for 12 h. Finally, Au NBP/a-TiO_2 was obtained by centrifugation and re-dispersed in water for use.

2.2.5. Temperature measurement under 808 nm laser irradiation

1 mL of blank DI water, or DI water solutions of TiO_2, Au NBP@SiO_2, or Au NBP/a-TiO_2 were irradiated with an 808 nm laser (2 W/cm^2) for 10 min, respectively, during which the temperature was measured every 20 s by a thermocouple (TC300P(K)).

2.2.6. ROS generation test

200 μL of blank DI water or DI water solutions of TiO_2, Au NBP@TiO_2 (annealed), Au NBP@SiO_2, or Au NBP/a-TiO_2 were added to 2 mL of RhB (5 μM) solution, and each sample was irradiated with an 808 nm laser (2 W/cm^2) in a water bath to prevent temperature elevation. The absorbance of each sample was measured with a UV-vis spectrometer at each time point.

2.2.7. Superoxide generation test

100 μL of blank DI water or DI water solutions of TiO_2, Au NBP@TiO_2 (annealed), Au NBP@SiO_2, or Au NBP/a-TiO_2 were added to 3 mL of hydroethidine (33 μM) solution and each sample was irradiated with an 808 nm laser (2 W/cm^2) in a water bath to prevent temperature elevation. Finally, each sample was centrifuged and photoluminescence was measured from the supernatant.

2.2.8. Hydroxyl radical generation test

Electron paramagnetic resonance (EPR) spectra of the spin adducts were acquired on a Bruker EMX spectrometer operating at room temperature, a microwave frequency of 9.64 GHz, and a 100-kHz field modulation (KBSI western center, Seoul, Korea). Before measurement, each sample (100 μL) was mixed with a DMPO solution (1 μL) and subsequently irradiated with an 808 nm laser (2 W/cm^2) for 25 min. A small amount of the solution was transferred to a glass tube and subjected to the EPR measurement.

2.2.9. In vitro *cytotoxicity test*

Human glioblastoma (U-87 MG) cells were obtained from a Korean Cell Line Bank. U-87 MG cells were cultured in Dulbecco's Modified Eagle's Medium (DMEM) containing fetal bovine serum (10%) and antibiotic-antimycotic solution (1%) in a humidified cell culture incubator 5% CO2 at 37 °C. For cytotoxicity evaluation, cells were seeded on each well of a 96-well plate at a density of 1×10^4 cells/well and cultured in DMEM for 24 h. The cells were

washed with DPBS, and then Au NBP@SiO_2, a mixture of Au NBP@SiO_2 and TiO_2 (Au NBP@SiO_2 + TiO_2), TiO_2 or Au NBP/a-TiO_2 in DMEM was added to each well. For each sample, the concentration was adjusted to the optical density (OD) of 0.2 at 808 nm. After 24 h incubation, cells were washed with DPBS and recharged with fresh DMEM. For phototoxicity, each well was irradiated with an 808 nm laser for 3 min and the cells were further incubated for 24 h. After DPBS washing, cell viability was evaluated by the MTT assay. For flow cytometry, cells were stained with Annexin-AM and PI co-staining solution for 20 min.

2.2.10. In vitro *live cell imaging*

U-87 MG cells were incubated with Au NBP@SiO_2, Au NBP@SiO_2 + TiO_2, TiO_2, and Au NBP/a-TiO_2 for 24 h, respectively (OD 0.2 at 808 nm for each). After DPBS washing, the cells were irradiated with an 808 nm laser for 3 min except for the dark condition and further incubated for 24 h. The treated cells were washed with DPBS and stained with calcein-AM live cell staining solution for 15 min. All fluorescence images were obtained by using a Nuance FX multispectral imaging system (Cambridge Research & Instrumentation, Inc., USA). To image the ROS generation *in vitro*, cells were stained with DCFH-DA.

2.2.11. In vivo *test*

All animal experiments were proceeded based on the relevant laws and institutional guidelines of the Korea Institute of Science and Technology (KIST) and institutional committees (approval number: KIST-2020-073). For preparation of tumor models, BALB/c nude mice (male, 5 weeks of age, Orient Bio Inc. Korea) were anaesthetized by the inhalation of isoflurane liquid. Tumor xenografts were created by subcutaneous injection of a suspension of U- 87 MG cells (1×10^7 cells in 60 μL of culture medium) into the thigh of mice. After xenograft model preparation (2 weeks), Au NBP@SiO_2, Au NBP@SiO_2 + TiO_2, TiO_2 and Au NBP/a-TiO_2 or PBS solution

was carried out (60 μL total injection volume per mouse) by intratumoral injection. Each group of the U-87 MG tumor bearing mice were exposure to NIR laser (808 nm, 2 W/cm^2) for 5 min. The tumor volume was measured by a digital caliper and calculated (width × length × height × 1/2) for 32 d.

2.2.12. Histological analysis

The major organs were collected from U-87 MG tumor xenograft mice treated with Au NBP@SiO_2, Au NBP@SiO_2 + TiO_2, TiO_2 and Au NBP/a-TiO_2 or PBS solution under laser irradiation 7 d after intratumoral injection. The organs were fixed with 4% formaldehyde solution. The sections were stained with hematoxylin and eosin (H&E) and terminal deoxynucleotidyl transferase dUTP nick end labeling (TUNEL).

3. Results and discussion

3.1. Structural and photophysical characterization.

The synthetic route is illustrated in Fig. 1a. Firstly, anisotropic Au NBP was synthesized by a seed-mediated method [23-25]. To improve the colloidal dispersity in the given solvent (EtOH/water mixture) during subsequent TiO_2 deposition, the Au NBP surface was coated with a silica layer of 2−5 nm thickness (Fig. S1). Among the various stabilizing ligands, such as thin silica layer, polyvinylpyrrolidone, polystyrene sulfonate, citric acid, and gum arabic, only thin silica layer prevented the agglomeration of Au NBP and improved the colloidal dispersity under the acidic condition (Fig. S2). Furthermore, ultra-thin silica layer was reported to improve photocatalytic effects [26]. Anatase TiO_2 was then directly grown onto the resulting Au NBP@SiO_2 surface under a mild low-temperature hydrothermal condition at 80 °C, without additional high-temperature annealing.

Transmission electron microscopy (TEM) analysis revealed that the as-synthesized anisotropic Au NBP has a sharp-tipped morphology with a dimension of 100 nm × 30 nm (aspect ratio ~3.3) (Fig. S2). The morphology after TiO_2 deposition (Au NBP/a-TiO_2) was shown to incorporate nanoclusters of ~10 nm TiO_2 coated on the Au NBP surface (Fig. 1b). TEM images clearly evidenced that the original sharp tip of the Au NBP core remained intact with no sign of morphological disruption. The hybrid structure of Au NBP/a-TiO_2 was further verified by energy-dispersive X-ray (EDX) elemental mapping that reveals the spatial distribution of Au in the core and Ti in the periphery (Fig. 1c). Selected area electron diffraction (SAED) patterns corroborated the formation of anatase phase (Fig. S3), where the d-spacing at 0.3625, 0.2382, 0.189, 0.1701, 0.1489, 0.1379, and 0.1273 nm correspond to the anatase crystal planes of {101}, {004}, {200}, {105}, {204}, {116}, and {215}, respectively [27].

For comparison, a typical anatase crystallization by high-temperature treatment was conducted with Au NBP@amorphous TiO_2 by following the typical literature procedure (e.g., annealing at 250 °C for 24 h, see Supporting Information for details) [5]. As shown in Fig. 1d, the annealed Au NBP@TiO_2 revealed extensive particle agglomeration by the interparticle TiO_2 fusion, indicating a significant decline in the colloidal dispersity. Moreover, as anticipated from the thermal instability of Au NBP, the Au core tips were irregularly blunted after high-temperature annealing (Fig. 1e), which is in contrast to the tip sharpness preserved during the low-temperature hydrothermal reaction in the case of Au NBP/a-TiO_2 (Fig. 1f). The degree of Au tip disruption depending on the reaction condition was quantified by comparing the Au areas in the pyramidal region before and after the reaction (Fig. S4). Under the typical high-temperature annealing condition, the Au area was reduced by 19% compared to parent bare Au NBP, indicating the occurrence of a significant morphological change. However, the mild low-

temperature hydrothermal reaction resulted in only 1% reduction of Au area, validating its synthetic compatibility with thermally unstable anisotropic gold nanostructures. Taken together, our novel mild temperature hydrothermal method maintains their sharp-tip morphology. This strategy resulted in preservation of strong electric field enhancement and hot electron generation ability of Au NBP, leading to enhancement of plasmonic photocatalytic effect of Au NBP/a-TiO_2.

The formation of anatase in Au NBP/a-TiO_2 was further corroborated by the X-ray diffraction (XRD) measurement. As shown in Fig. 1g, Au NBP@amorphous TiO_2 only exhibited peaks attributed to the {111}, {200}, and {220} facets of the metallic gold phase. In sharp contrast, Au NBP/a-TiO_2 revealed additional diffraction peaks at 25.2° and 48.4°, which correspond to the {101} and {200}) planes of anatase [28]. This concludes that anatase TiO_2 was directly deposited on the Au surface without a separate harsh step of high-temperature annealing.

The light absorption properties of plasmonic Au NBP were then assessed comparatively depending on the reaction condition (Fig. 1h). The longitudinal and transverse surface plasmon resonance (SPR) peaks of pristine Au NBP were found at ~768 and ~505 nm, respectively, in line with previous reports by our group [29]. After high-temperature annealing of Au NBP@amorphous TiO_2, the characteristic intense and narrow longitudinal band at ~768 nm declined significantly with spectral broadening, attributed to the morphology disruption of Au NBP as evidenced in Fig. 1e. In the case of sharp tip-conserved Au NBP/a-TiO_2 prepared under the low-temperature hydrothermal condition, however, the longitudinal SPR peak was shown to be still intense with no significant spectral change, indicating the importance of plasmonic shape preservation to take advantage of plasmon resonance-enhanced optical properties. A slight red shift of ~18 nm and broadening to the longer-wavelength NIR side observed with Au NBP/a-TiO_2 are likely attributed to the surface environment change of Au NBP due to the presence of

anatase TiO_2 with a distinct refractive index [30,31].

3.2. Photocatalytic and photothermal properties.

Preserving the NIR-responsive plasmonic optical properties of anisotropic Au NBP, Au NBP/a-TiO_2 exhibited the almost intact photothermal effect for light-activated heat generation (Fig. 2a). Under laser irradiation at 808 nm, parent sharp-tipped Au NBP (Au NBP@SiO_2, a precursor of Au NBP/a-TiO_2) heated its aqueous dispersion to reach the maximum temperature at 60 °C within ~5 min, which is far higher than those of bare TiO_2 and blank water (< 40 °C). The observed photothermal effect is ascribable to efficient non-radiative thermal deactivation of the sharp-tipped plasmonic nanostructure upon photoexcitation [32]. Likewise, water-dispersed Au NBP/a-TiO_2 revealed a similarly efficient temperature rise up to 57 °C under the given irradiation condition, further supporting the merit of our mild anatase deposition condition for preserving the plasmonic properties of highly anisotropic gold nanostructures. Importantly, Au NBP/a-TiO_2 exhibited a highly stable photothermal behavior during the repeated heating/cooling cycles by turning the 808 nm laser on and off (Fig. S5), suggesting the structural stability for potentiating repeated and prolonged photothermal applications.

Further experiments were then performed to evaluate the plasmonic hybridization-induced UV-to-NIR spectral modulation of anatase TiO_2 for the photocatalytic response. The production of ROS was monitored with rhodamine B (RhB) that is a typical indicator known to lose its absorption under the ROS-rich oxidative condition [33]. Fig. 2b shows the concentration evolutions of RhB in the presence of various samples during NIR irradiation at 808 nm, where only Au NBP/a-TiO_2 displayed extensive gradual photobleaching of RhB, in contrast to negligible degradation by unhybridized UV-responsive anatase TiO_2 and non-photocatalytic Au NBP (Au NBP@SiO_2). Without laser excitation, no degradation of RhB was observed in all the

cases (Fig. S6). All these results indicate remarkable ROS generation by hybridized Au NBP/a-TiO_2 in response to the NIR excitation, evidencing efficient oxygen reduction by facile injection of LSPR-derived hot electrons from the sharp-tipped Au NBP surface to the thin anatase nanocluster shell as proposed in Scheme 1 [5,32]. In the case of typically synthesized Au NBP@TiO_2 by high-temperature annealing, no noticeable photocatalytic ROS generation was observed in spite of plasmonic hybridization and anatase formation. This is presumably because the thick shell formed by interparticle TiO_2 fusion (Fig. 1d) hinders the transport of hot electrons from the plasmonic interface to the outer surface of TiO_2 where oxygen reduction occurs, and also because the blunted gold tips during annealing (Fig. 1e) deteriorate the LSPR effect [7]. To our interest, a simple mixture of Au NBP@SiO_2 and anatase TiO_2 (Au NBP@SiO_2 + TiO_2) also exhibited a notable sign of ROS generation with ~58% photobleaching of RhB after 24 h NIR irradiation (Fig. S7), which is opposed to negligible bleaching by each of them separately (Fig. 2b). This is likely attributed to the nonspecific random adsorption between them to facilitate the injection of NIR-excited plasmonic hot electrons into the photocatalytic anatase, corroborating the important role of heterospecies interfacing to potentiate hybrid functions. Under the same condition, Au NBP/a-TiO_2 revealed much more RhB photobleaching (~96%, Fig. S7), suggesting that our mild hydrothermal reaction approach enables efficient interfacing and close contact between Au NBP and anatase in a more controlled manner.

According to the proposed mechanism in Scheme 1, the details of photocatalytic ROS generation were examined with NIR-excited Au NBP/a-TiO_2. Firstly, the generation of superoxide ($O_2^{\cdot-}$) was confirmed with hydroethidine (HE), a fluorogenic indicator that selectively generates fluorescence at 630 nm in response to $O_2^{\cdot-}$ [34]. Among other control samples, only Au NBP/a-TiO_2 displayed a notable fluorogenic response of the $O_2^{\cdot-}$ generation

under 808 nm laser irradiation (Figs. 2c and S8). Likewise, the NIR-excited $O_2^{\cdot-}$ generation was evident with the randomly adsorbed mixture of Au NBP@SiO_2 and anatase TiO_2 (Au NBP@SiO_2 + TiO_2, Fig. S9). All these results are well accordant with the findings of general ROS generation examined by RhB photobleaching (Figs. 2b and S7), suggesting that $O_2^{\cdot-}$ is among primary ROS involved in the NIR-responsive photocatalytic activity of Au NBP/a-TiO_2. As the second candidate of ROS, the generation of hydroxyl radicals (·OH) were monitored by electron paramagnetic resonance (EPR) analysis in the presence of 5,5-dimethyl-1-pyrroline N-oxide (DMPO), a well-established trapping agent for ·OH [35]. As revealed in Fig. 2d, four characteristic peaks corresponding to ·OH became more obvious upon NIR excitation of Au NBP/a-TiO_2, indicating that its photocatalytic ROS generation involves ·OH as well.

3.3. In vitro *cancer therapeutic effect test.*

Having confirmed the efficient plasmonic (photothermal and photocatalytic) activities in the NIR, we explored the biomedical potential of Au NBP/a-TiO_2 by applying it to locoregional phototherapy of cancer. Fig. 3 comparatively shows the NIR-activated anticancer activities of various samples examined *in vitro* with human glioblastoma cells (U-87 MG). Firstly, the cellular uptake was assessed by dark-field microscopic imaging of sample-treated cells, where Au NBP/a-TiO_2 revealed the most intracellularly localized scattering signals over other control samples (Fig. S10). This behavior is well accordant to the literature report that stably dispersed TiO_2-coated gold nanomaterials are avidly taken up by U-87 MG cells [36]. After sample treatment, cytotoxicity was assessed by the MTT assay in the presence and absence of laser excitation at 808 nm. Without light exposure, no obvious cytotoxicity was observed with all the samples under the given condition (Fig. 3a). In particular, the cells treated with Au NBP/a-TiO_2 remained viable up to the Au dose of 23 μg/mL (corresponding to optical density of 0.4 at 808

nm), demonstrating its biocompatibility with minimal toxicity in the absence of light (Fig. S11).

Fig. 3b shows the phototoxicity examined under 808 nm laser irradiation. It is obvious that the viabilities of untreated cells and cells treated with UV-responsive anatase TiO_2 were intact under NIR exposure, whereas Au NBP-containing samples imposed moderate-to-severe phototoxic impacts on the treated cells to a varying degree depending on the sample composition. The moderate toxicity observed with non-photocatalytic Au NBP@SiO_2 suggests that its photothermal heating effect (Fig. 2a) affected the cell viability to that extent (~83% viability) under the given irradiation condition. In the case of a simple mixture of Au NBP@SiO_2 and anatase TiO_2 (Au NBP@SiO_2 + TiO_2), additional phototoxicity was attained (~75% viability), unambiguously attributable to the cytotoxic ROS generation by NIR photocatalysis contributed from the heterospecies close contact by random adsorption as discussed above (Figs. S7 and S9). Such an additional ROS-generating photocatalytic contribution to the phototoxicity was significantly more pronounced with Au NBP/a-TiO_2 (~37% viability), evidencing potential of its elaborately controlled hybrid nanostructure for LSPR-induced NIR photodynamic therapy.

The observed phototoxic behaviors were further confirmed by cell viability imaging with calcein-AM, a fluorogenic indicator that becomes fluorescent in response to the esterase-rich environment only in viable cells [37]. As shown in Figs. 3c and S12, green fluorescence signals from fluorescently converted calcein-AM were observed in all the control groups to varying degrees, whereas such a viability signal was relatively negligible in the group treated with Au NBP/a-TiO_2 + laser unambiguously due to the declined esterase activities of the photodamaged cells, well reflecting the above MTT results. To have an insight into the observed phototoxicity, flow cytometric analysis was performed by dual staining of the treated cells with annexin V-FITC and propidium iodide (PI), where the former and the latter stain apoptotic and necrotic

cells, respectively (Figs. 3d and S13) [38]. The resulting quadrant graphs revealed that the photothermal-only group (Au NBP@SiO_2) caused minor amounts of early apoptosis (annexin V positive/PI negative, lower right quadrant) and late apoptosis/necrosis (annexin V positive/PI positive, upper right quadrant) while keeping the majority viable (annexin V negative/PI negative, lower left quadrant). In the case of a simple mixture (Au NBP@SiO_2 + TiO_2), the additional photocatalytic toxicity could be proven by the increased cell populations in both the lower right and upper right quadrants. Importantly, the phototreatment with Au NBP/a-TiO_2 under the same condition increased exceptionally the population of late apoptotic/necrotic cells in the upper right quadrant over healthy and early apoptotic cells. These results are in good agreement with the tendency of intracellular ROS generation. Under microscopic observation with staining of a fluorogenic ROS indicator (DCFH-DA) [39], obvious green signals responsive to ROS were seen only in the Au NBP/a-TiO_2-treated cells among other controls (Figs. 3e and S14). Taken together, it is concluded that elaborate nanohybridization achieved in Au NBP/a-TiO2 potentiates NIR-responsive ROS generation that is efficient enough to impose a robust anticancer impact with efficient cellular uptake and cytotoxicity, being useful for photodynamic therapy.

3.4. In vivo *cancer therapeutic effect test.*

The phototherapeutic potential of Au NBP/a-TiO_2 was further validated *in vivo* with U-87 MG tumor-bearing mice, for which samples were injected intratumorally (Fig. 4). It was clearly shown that all the tumor-injected samples have no sign of anticancer activity in the absence of light (Fig. S15), while some of them responded to the NIR irradiation. As shown in the *in vivo* thermograms and temperature rise profiles obtained with 808 nm laser irradiation of the tumors for 5 min (Figs. 4a,b and S16), Au NBP-containing groups exhibited temperature rises, which

agrees well with their photothermal behaviors examined *in vitro* (Fig. 2a). In line with the observed photothermal effect, only Au NBP-containing samples retarded the tumor growth significantly, as opposed to no therapeutic effect from other NIR-inactive control groups under the same NIR phototreatment condition (Figs. 4c and S15). Importantly, nanohybrid Au NBP/a-TiO_2 revealed remarkably more pronounced tumor growth inhibition than the others having similar photothermal effects (Au NBP@SiO_2 and Au NBP@SiO_2 + TiO_2), strongly supporting the plasmon-enhanced photocatalytic contribution.

For further *ex vivo* examination and histological analysis, all the treated tumor tissues were collected after sacrifice. Figs. 4d and S17 show the resected tumor sizes comparatively. In all the laser-untreated control groups, tumors were aggressively grown. Likewise, laser-treated but NIR-inactive groups (DI water and TiO_2-treated models) also revealed tumor growth to a similar extent. On the contrary, all the Au NBP-containing samples resulted in tumor suppression under NIR laser irradiation. As revealed by hematoxylin and eosin (H&E) staining and terminal deoxynucleotidyl transferase dUTP nick end labeling (TUNEL) assay (Figs. 4e,f and S18-19), all the laser-treated groups with Au NBP-containing samples showed notable tissue and DNA damages by apoptosis. In particular, Au NBP/a-TiO_2 manifested a much higher level of laser-induced apoptosis than other controls (Au NBP@SiO_2 and Au NBP@SiO_2 + TiO_2). Considering that the tumor growth inhibition by non-photocatalytic Au NBP@SiO_2 is entirely caused by its photothermal effect, the enhanced anticancer efficacy observed with Au NBP/a-TiO_2 is unambiguously attributed to an additional contribution from the NIR-activated photocatalytic ROS generation achieved by the successfully synthesized hybrid nanostructure. It is noted that Au NBP@SiO_2 + TiO_2 did not show such additional photocatalytic enhancement in the tumor-suppressing effect, suggesting that the simply adsorbed structure is not stable enough to be

operative for NIR-responding ROS generation in the *in vivo* environment. Finally, the phototreated group with Au NBP/a-TiO_2 exhibited a 100% survival rate even after 54 d, in striking contrast to other groups that showed declined survival rates after 34 d (Fig. S20), further corroborating the enhanced anticancer phototherapeutic effect of Au NBP/a-TiO_2.

3.5. Safety evaluation.

It is noted that the nanostructures investigated herein exhibited minimal toxic impacts on the mouse viability with negligible body weight loss during the examined period of 16 d (Fig. S21). Importantly, no obvious tissue damages were detected in the H&E-stained sections of major organs resected from the phototreated mice with Au NBP/a-TiO_2 (Fig. S22). Moreover, the blood test attributes were almost the same as those of normal mice within a range of clinical standard for mice (Fig. S23). All these results on the *in vivo* toxicity studies elucidate the biocompatibility and biomedical promise of our Au NBP/a-TiO_2 nanohybrid.

4. Conclusions

In summary, we developed a novel synthetic method for hybridizing sharp-tipped Au NBP and anatase TiO_2 to produce Au NBP/a-TiO_2 with application in combinational photothermal and photodynamic cancer therapy. The low temperature hydrothermal condition introduced here could enable the direct crystalline deposition of anatase TiO_2 onto the gold surface without morphological disruption of Au NBP and agglomeration of the resulting core/shell nanohybrid. Only 1% reduction of Au area was observed with our novel mild temperature hydrothermal method unlike 19% Au area reduction of typical method, i.e., high-temperature annealing of the pre-deposited amorphous TiO_2 shell. Under the NIR excitation, the shape-conserved Au NBP core could effectively produce plasmonic hot electrons and directly inject them into the

conduction band of the hybridized anatase TiO_2 shell, leading to significant improvement of NIR-responsive photocatalytic activities compared to a control (annealed Au NBP@TiO_2) that was prepared by a typical method. 96% of the RhB photobleaching was detected with newly synthesized Au NBP/a-TiO_2, whereas negligible photobleaching was observed with typical Au NBP@TiO_2. By virtue of the plasmonic morphology conservation, Au NBP/a-TiO_2 also exhibited the NIR-responsive LSPR-induced photothermal effect as excellent as the pristine sharp-tipped Au NBP core. *In vitro* and *in vivo* studies demonstrated that the combination of photothermal and photocatalytic contributions within a single nanohybrid framework, along with the improved colloidal dispersity, holds potential for phototherapy of cancer. We conclude that our nanohybrid methodology for preparing Au NBP/a-TiO_2 may provide a new synthetic strategy to expand the spectrum of NIR-responsive photocatalytic hybrid nanostructures for biomedical applications.

Credit author statement

D. H. Kim conceived the concept and supervised the project. D. Jang developed the concrete strategies, conducted the main experiments, analyzed the data, and wrote the manuscript. S. Kim provided the experimental facilities and supervised the project. S. Yu, K. Chung, J. Yoo, F. Marques Mota, J. Wang, D. J. Ahn assisted the synthesis of the constituent components of the hybrid nanostructures and part of the diverse property tests. All the authors discussed the results and contributed to the preparation of the manuscript.

Declaration of competing interest

The authors declare that they have no known competing financial interests or personal relationships that could have appeared to influence the work reported in this paper.

Acknowledgments

This work was supported by National Research Foundation of Korea Grant funded by the Korean Government (NRF-2020R 1A 2C 3003958), by Basic Science Research Program (Priority Research Institute) through the National Research Foundation of Korea (NRF) funded by the Ministry of Education (2021R 1A 6A 1A10039823), by Korea Basic Science Institute (National Research Facilities and Equipment Center) grant funded by the Ministry of Education (2020R 1A 6C 101B194) and by Creative Materials Discovery Program through the NRF of Korea funded by Ministry of Science and ICT (2018M 3D 1A 1058536). The work at Korea Institute of Science and Technology was supported by funds from the National Research Foundation of Korea (2017M3A9D8029942 and 2021R1A2C2005418), and the KIST intramural program. The authors would also like to thank the Korean Basic Science Institute (KBSI) at the Western Seoul center for EPR measurements.

Appendix A. Supplementary data

Supplementary data to this article can be found online at

FIGURES

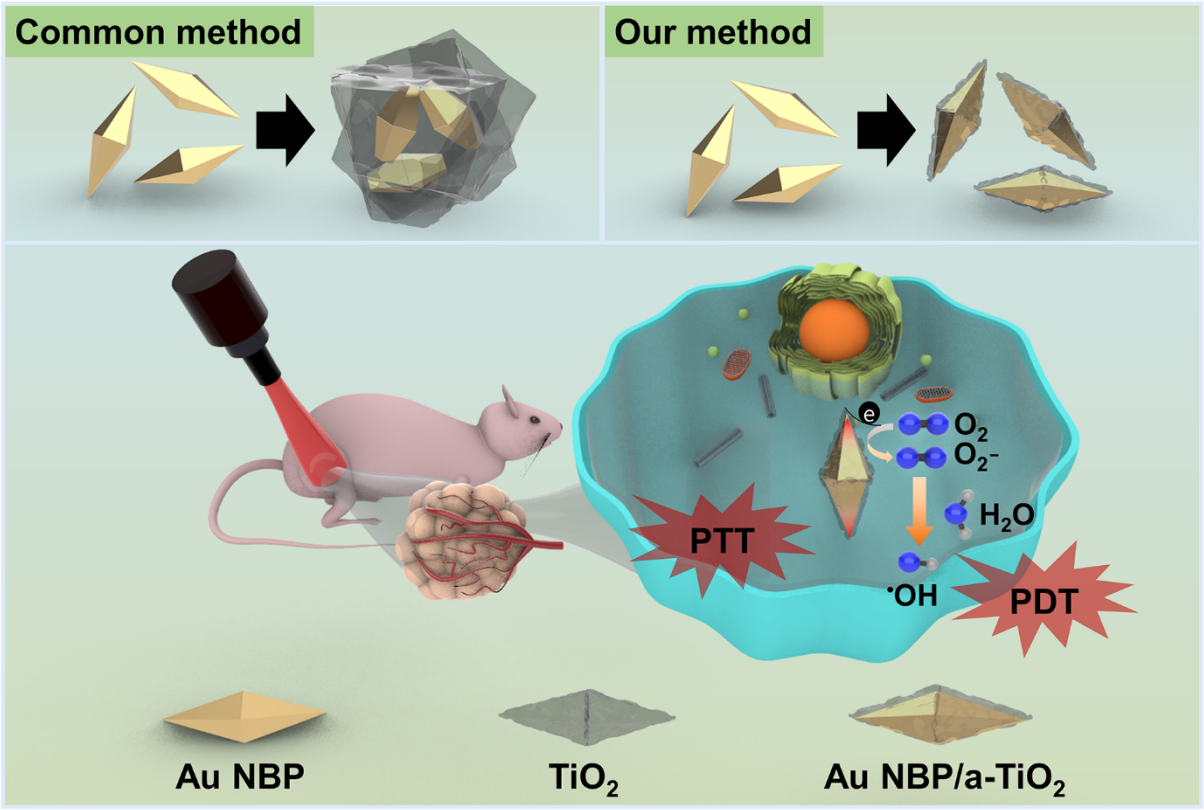

Scheme 1. Schematic diagram for the combinational photothermal and photocatalytic cancer treatment using morphology-conserved plasmonic nanohybrid structures prepared by unconventional direct deposition of TiO_2 on thermally unstable Au NBP core-shell nanostructures under the 808 nm laser irradiation.

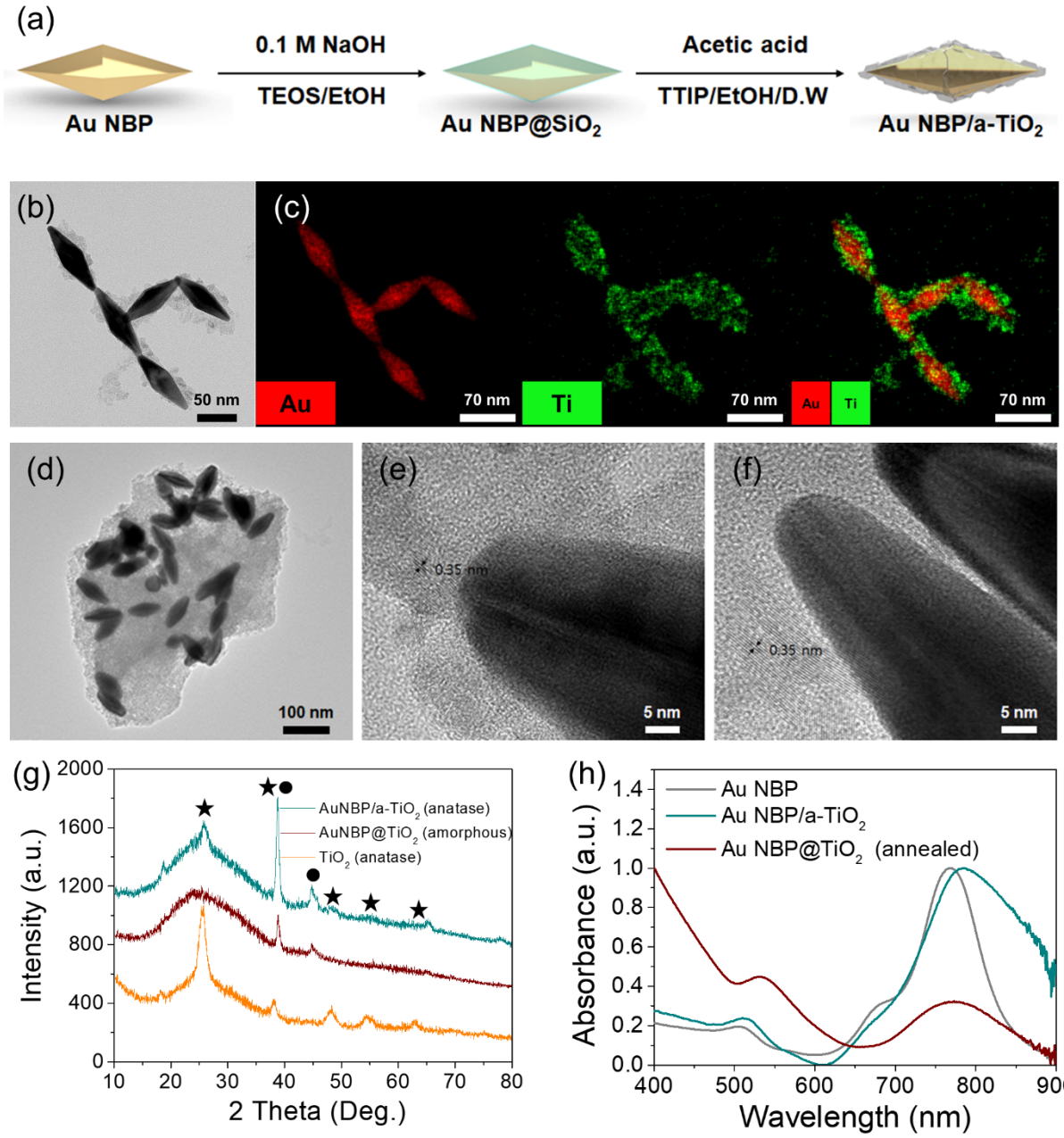

Fig. 1 Structural characterizations. (a) Schematic illustration of overall synthesis process of Au NBP/a-TiO_2. (b) TEM image of Au NBP/a-TiO_2. Scale bar, 50 nm. (c) EDX elemental mapping data of Au, Ti and merged. Scale bar, 70 nm. (d, e) TEM and HRTEM images of annealed Au NBP@TiO_2 at 250 °C for 24 h. Scale bar, 100 nm and 5 nm, respectively. (f) HRTEM image of Au NBP/a-TiO_2. Scale bar, 5 nm. (g) XRD patterns of Au NBP/a-TiO_2, Au NBP@TiO_2 (amorphous), and anatase TiO_2. Star and circle marks indicate anatase TiO_2 and Au, respectively. (h) Normalized UV-Vis absorbance spectra of Au NBP, Au NBP/a-TiO_2, and annealed Au NBP@TiO_2

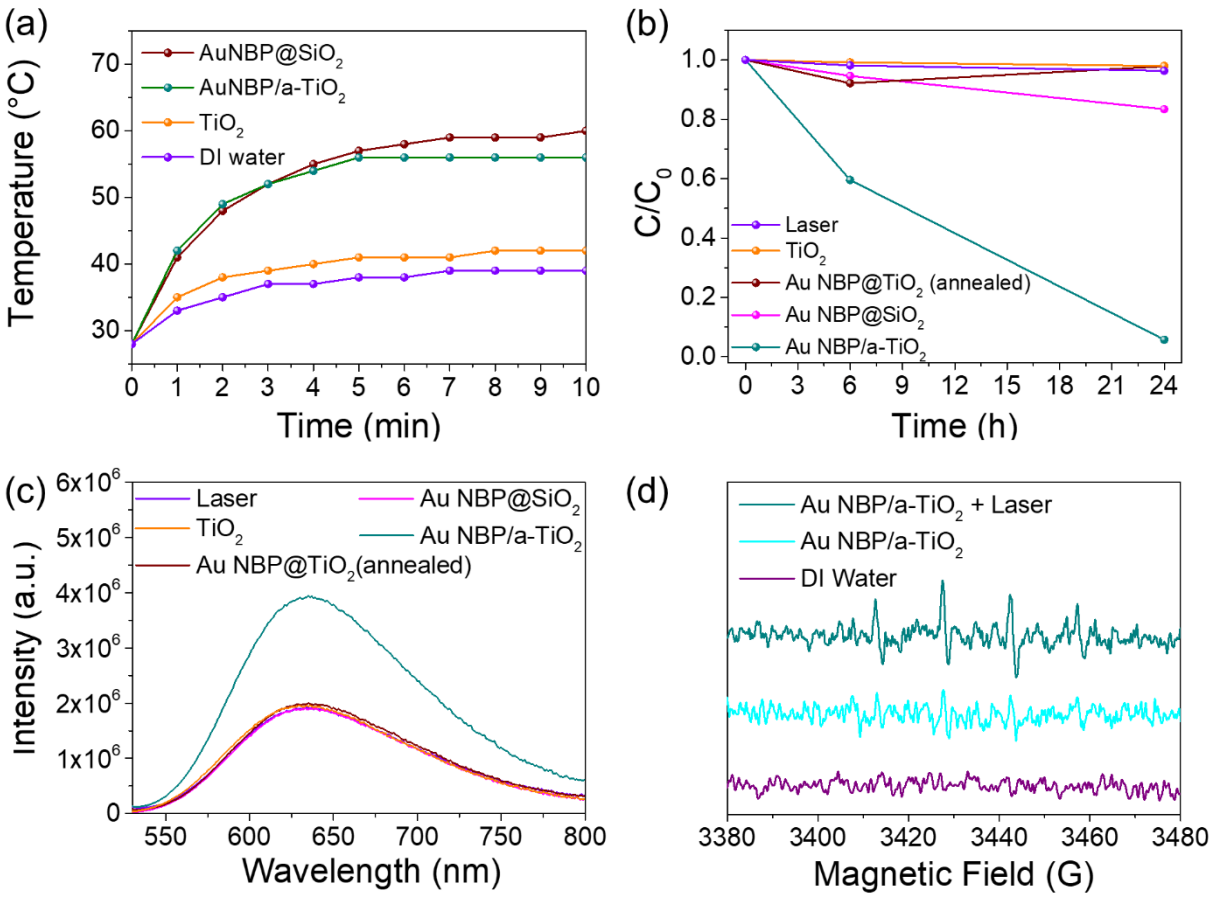

Fig. 2 Therapeutic effects. (a) Time-dependent temperature rising profile of Au NBP@SiO_2, Au NBP/a-TiO_2, neat TiO_2, and DI water under the 808 nm laser (2 W/cm^2) irradiation (b) UV-vis absorption spectra of RhB with DI Water, neat TiO_2, Au NBP@SiO_2, annealed Au NBP@TiO_2, and Au NBP/a-TiO_2 under the 808 nm laser (2 W/cm^2) irradiation. (c) Photoluminescence spectra of hydroethidine of DI water, neat TiO_2, Au NBP@SiO_2, annealed Au NBP@TiO_2, and Au NBP/a-TiO_2 under the 808 nm laser (2 W/cm^2) irradiation. (d) EPR signals of DMPO-OH adducts in presence of DI Water and Au NBP/a-TiO_2 with or without illumination of 808 nm laser (2 W/cm^2).

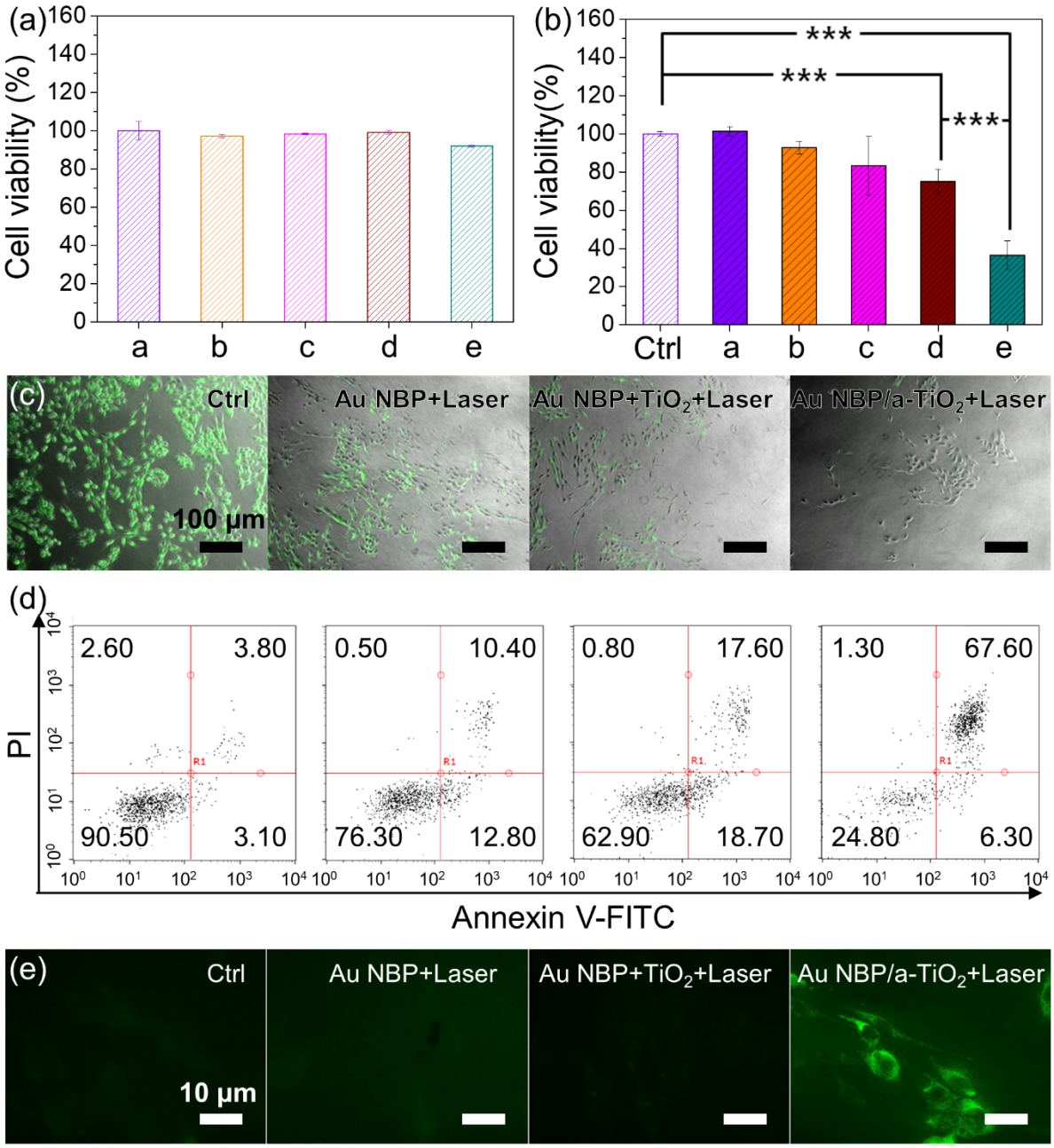

Fig. 3 *In vitro* cell viability and ROS generation test. (a) Cell viability under the dark condition (a: DI water, b: TiO_2, c: Au NBP@SiO_2, d: mixture of Au NBP@SiO_2 + TiO_2 and e: Au NBP/a-TiO_2). (b) Cell viability under 808 nm laser (2 W/cm^2) irradiation for 3 min. (a: DI water, b: TiO_2, c: Au NBP@SiO_2, d: mixture of Au NBP@SiO_2 + TiO_2 and d: Au NBP/a-TiO_2) (P values, *P < 0.05, **P < 0.01, ***P < 0.001). (c) Fluorescence images of calcein-AM stained U-87 MG cells incubated with DI Water, Au NBP@SiO_2, mixture of Au NBP@SiO_2 + TiO_2, and Au NBP/a-TiO_2 under 808 nm laser (2 W/cm^2) irradiation for 3 min. (d) Flow cytometry analysis of U-87 MG cells stained with Annexin V-FITC/PI early/late apoptosis staining solution incubated with (left to right) DI Water, Au NBP@SiO_2, mixture of Au NBP@SiO_2 + TiO_2, and Au NBP/a-TiO_2 under 808 nm laser (2 W/cm^2) irradiation for 3 min. (e) Fluorescence images of DCFH-DA

stained U-87 MG cells incubated with DI Water, Au NBP@SiO_2, mixture of Au NBP@SiO_2 + TiO_2, and Au NBP/a-TiO_2 under 808 nm laser (W/cm^2) irradiation for 3 min.

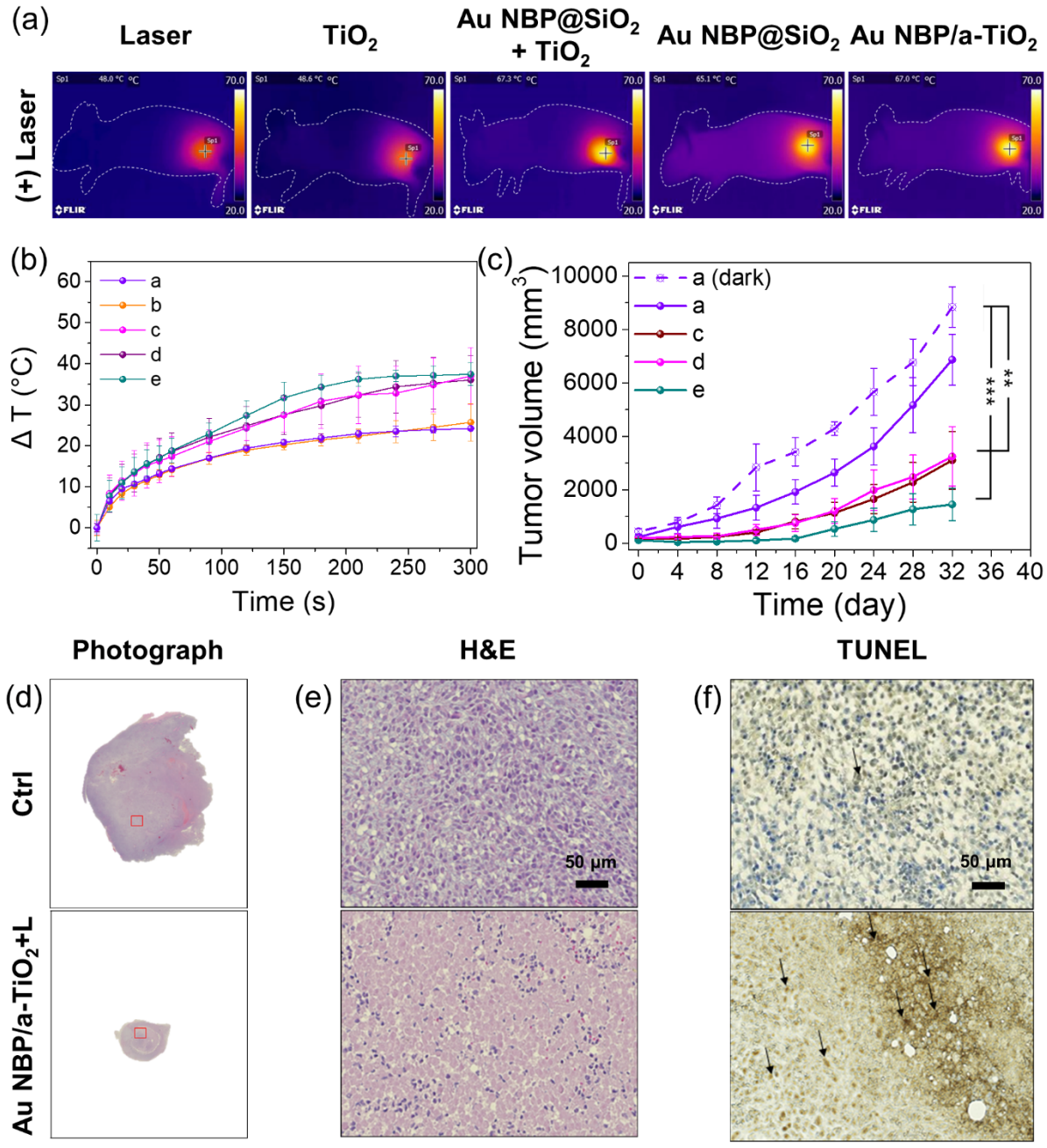

Fig. 4 *In vivo* antitumor efficacy. (a) Photothermal imaging of U-87 MG bearing mice treated with DI Water, TiO_2, Au NBP@SiO_2, mixture of Au NBP@SiO_2 + TiO_2, and Au NBP/a-TiO_2 under 808 nm laser (2 W/cm^2) irradiation for 5 min. (b) Tumor site time-dependent temperature rising profile. (c) Changes in the tumor volume with respect time (P values, *P < 0.05, **P < 0.01, ***P < 0.001). The samples were represented as follow: (a: DI water, b: TiO_2, c: Au NBP@SiO_2, d: mixture of Au NBP@SiO_2 + TiO_2, e: Au NBP/a-TiO_2). Dashed line and continuous line represented dark condition and 808 nm laser (2 W/cm^2) irradiation for 5 min, respectively). (d) Photograph of Tumor section stained with H&E staining solution after treatment of DI Water and Au NBP/a-TiO_2 under 808 nm laser (2 W/cm^2) irradiation for 5 min.

(e) H&E staining assay of the tumor tissue after treatment of DI Water and Au NBP/a-TiO_2 under 808 nm laser (2 W/cm^2) irradiation for 5 min. (f) TUNEL staining assay of the tumor tissue after treatment of DI Water and Au NBP/a-TiO_2 under 808 nm laser (2 W/cm^2) irradiation for 5 min.

REFERENCES

[1] H. C. Huang, S. Barua, G. Sharma, S. K. Dey, K. Rege, Inorganic nanoparticles for cancer imaging and therapy, J. Control. Release 155(3) (2011) 344-357. https://doi.org/10.1016/j.jconrel.2011.06.004.

[2] Y. Orooji, B. Tanhaei, A. Ayati, S. H. Tabrizi, M. Alizadeh, F. F. Bamoharram, F. Karimi, S, Salmanpour, J. Rouhi, S. Afshar, M. Sillanpää, R. Darabi, H. Karimi-Maleh, Heterogeneous UV-switchable Au nanoparticles decorated tungstophosphoric acid/TiO_2 for efficient photocatalytic degradation process. Chemosphere 281 (2021) 130795. https://doi.org/10.1016/j.chemosphere.2021.130795

[3] H. Karimi-Maleh, B. G. Kumar, S. Rajendran, J. Qin, S. Vadivel, D. Durgalakshmi, F. Gracia, M. Soto-Moscoso, Y. Orooji, F. Karimi, Tuning of metal oxides photocatalytic performance using Ag nanoparticles integration. J. Mol. Liq. 314 (2020) 113588. https://doi.org/10.1016/j.molliq.2020.113588

[4] M. Soleimani, J. B. Ghasemi, G. M. Ziarani, H. Karimi-Maleh, A. Badiei, Photocatalytic degradation of organic pollutants, viral and bacterial pathogens using titania nanoparticles, Inorg. Chem. Commun. 130, (2021) 108688. https://doi.org/10.1016/j.inoche.2021.108688

[5] C. Fang, H. Jia, S. Chang, Q. Ruan, P. Wang, T. Chen, J. Wang, (Gold core)/(titania shell) nanostructures for plasmon-enhanced photon harvesting and generation of reactive oxygen species, Energy Environ. Sci. 7(10) (2014) 3431-3438. doi: 10.1039/c4ee01787k.

[6] M. W. Knight, H. Sobhani, P. Nordlander, N. J. Halas, Photodetection with active optical antennas, Science 332(6030) (2011) 702-704. doi: 10.1126/science.1203056.

[7] Y. Ma, X. Zhu, S. Xu, G. He, L. Yao, N. Hu, Y. Su, J. Feng, Y. Zhang, Z. Yang, Gold nanobipyramid@cuprous oxide jujube-like nanostructures for plasmon-enhanced photocatalytic performance, Appl. Catal. B 234(15) (2018) 26-36. https://doi.org/10.1016/j.apcatb.2018.04.014.

[8] Z. Hou, Y. Zhang, K. Deng, Y. Chen, X. Li, X. Deng, Z. Cheng, H. Lian, C. Li, J. Lin, UV-emitting upconversion-based TiO_2 photosensitizing nanoplatform: near-infrared light mediated *in vivo* photodynamic therapy via mitochondria-involved apoptosis pathway, ACS Nano 9(3) (2015) 2584-2599. https://doi.org/10.1021/nn506107c.

[9] T. Luttrell, S. Halpegamage, J. Tao, A. Kramer, E. Sutter, M. Batzill, Why is anatase a better photocatalyst than rutile?-Model studies on epitaxial TiO_2 films, Sci. Rep. 4(4043) (2014) 1-8. https://doi.org/10.1038/srep04043.

[10] S. Kohtani, A. Kawashima, H. Miyabe, Reactivity of trapped and accumulated electrons in titanium dioxide photocatalysis, Catalysts 7(10) (2017) 303. https://doi.org/10.3390/catal7100303.

[11] T. Umebayashi, T. Yamaki, H. Itoh, K. Asai, Band gap narrowing of titanium dioxide by sulfur doping, Appl. Phys. Lett. 81(3) (2002) 454-456. https://doi.org/10.1063/1.1493647.

[12] K. Nagaveni, M. S. Hegde, N. Ravishankar, G. N. Subbanna, G. Madras, Synthesis and structure of nanocrystalline TiO_2 with lower band gap showing high photocatalytic activity, Langmuir 20(7) (2004) 2900-2907. https://doi.org/10.1021/la035777v.

[13] J. S. Lee, K. H. You, C. B. Park, Highly photoactive, low bandgap TiO_2 nanoparticles wrapped by graphene, Adv. Mater. 24(8) (2012) 1084-1088. https://doi.org/10.1002/adma.201104110.

[14] J. Lee, Y. H. Lee, J. S. Choi, K. S. Park, K. S. Chang, M. Yoon, Hydrothermal synthesis of defective TiO_2 nanoparticles for long-wavelength visible light-photocatalytic killing of cancer

cells, RSC Adv. 5(121) (2015) 99789-99796. doi: 10.1039/c5ra19045b
[15] J. Lee, Y. H. Lee, C. B. Jeong, J. S. Choi, K. S. Chang, M. Yoon, Gold nanorods-conjugated TiO_2 nanoclusters for the synergistic combination of phototherapeutic treatments of cancer cells, J. Nanobiotechnology 16(104) (2018) 1-12. https://doi.org/10.1186/s12951-018-0432-4.
[16] T. Zheng, W. Wang, F. Wu, M. Zhang, J. Shen, Y. Sun, Zwitterionic polymer-gated Au@TiO_2 core-shell nanoparticles for imaging-guided combined cancer therapy, Theranostics 9(17) 2019 5035-5048. doi: 10.7150/thno.35418.
[17] D. A. Hanaor, C. C. Sorrell, Review of the anatase to rutile phase transformation, J. Mater. Sci. 46(4) (2011) 855-874. https://doi.org/10.1007/s10853-010-5113-0.
[18] X. Kou, W. Ni, C. K. Tsung, K. Chan, H. Q. Lin, G. D. Stucky, J. Wang, Growth of gold bipyramids with improved yield and their curvature□directed oxidation, Small 3(12) (2007) 2103-2113. https://doi.org/10.1002/smll.200700379.
[19] S. Atta, A. M. Pennington, F. E. Celik, L. Fabris, TiO_2 on gold nanostars enhances photocatalytic water reduction in the near-infrared regime, Chem 4(9) (2018) 2140-2153. https://doi.org/10.1016/j.chempr.2018.06.004.
[20] J. L. Chen, H. Zhang, X. Q. Huang, H. Y. Wan, J. Li, X. X. Fan, K. Q. Luo, J. Wang, X. M. Zhu, J. Wang, Antiangiogenesis-combined photothermal therapy in the second near-infrared window at laser powers below the skin tolerance threshold, Nano-Micro lett. 11(93) (2019) 1-20. https://doi.org/10.1007/s40820-019-0327-4.
[21] H. Y. Wan, J. L. Chen, X. Zhu, L. Liu, J. Wang, X. M. Zhu, Titania□coated gold nano□bipyramids for blocking autophagy flux and sensitizing cancer cells to proteasome inhibitor□induced death, Adv. Sci. 5(3) (2018) 1700585. https://doi.org/10.1002/advs.201700585.
[22] J. Goebl, J. B. Joo, M. Dahl, Y. Yin, Synthesis of tailored Au@TiO_2 core–shell nanoparticles for photocatalytic reforming of ethanol, Catal. Today 225(15) (2014) 90-95. https://doi.org/10.1016/j.cattod.2013.09.011.
[23] Q. Li, X. Zhuo, S. Li, Q. Ruan, Q. H. Xu, J. Wang, Production of monodisperse gold nanobipyramids with number percentages approaching 100% and evaluation of their plasmonic properties, Adv. Opt. Mater. 3(6) (2015) 801-812. https://doi.org/10.1002/adom.201400505.
[24] M. Liu, P. Guyot-Sionnest, Mechanism of silver (I)-assisted growth of gold nanorods and bipyramids. J. Phys. Chem. B 109(47) (2005) 22192-22200. https://doi.org/10.1021/jp054808n.
[25] X. Kou, S. Zhang, C. K. Tsung, M. H. Yeung, Q. Shi, G. D. Stucky, L. Sun, J. Wang, C. Yan, Growth of gold nanorods and bipyramids using CTEAB surfactant. J. Phys. Chem. B 110(33) (2006) 16377-16383. https://doi.org/10.1021/jp0639086.
[26] X. Zhang, Y. Zhu, X. Yang, S. Wang, J. Shen, B. Lin, C. Li, Enhanced visible light photocatalytic activity of interlayer-isolated triplex Ag@SiO_2@TiO_2 core–shell nanoparticles. Nanoscale 5(8) (2013) 3359-3366. DOI: 10.1039/C3NR00044C.
[27] J. Lee, M. C. Orilall, S. C. Warren, M. Kamperman, F. J. Disalvo, U. Wiesner, Direct access to thermally stable and highly crystalline mesoporous transition-metal oxides with uniform pores, Nat. Mater. 7(3) (2008) 222-228. https://doi.org/10.1038/nmat2111.
[28] J. Wang, J. Yu, X. Zhu, X. Z. Kong, Preparation of hollow TiO_2 nanoparticles through TiO_2 deposition on polystyrene latex particles and characterizations of their structure and photocatalytic activity, Nanoscale Res. Lett. 7(1) (2012) 1-8. https://doi.org/10.1186/1556-276X-7-646.
[29] J. E. Kim, J. H. Choi, M. Colas, D. H. Kim, H. Lee, Gold-based hybrid nanomaterials for biosensing and molecular diagnostic applications, Biosens. and Bioelectron. 80(15) (2016) 543-559. https://doi.org/10.1016/j.bios.2016.02.015.

[30] J. Zhu, F. Zhang, J. J. Li, J. W. Zhao, Optimization of the refractive index plasmonic sensing of gold nanorods by non-uniform silver coating, Sens. Actuators B Chem. 183(5) (2013) 556-564. https://doi.org/10.1016/j.snb.2013.04.042.
[31] S. F. Kou, W. Ye, X. Guo, X. F. Xu, H. Y. Sun, J. Yang, Gold nanorods coated by oxygen-deficient TiO_2 as an advanced photocatalyst for hydrogen evolution, RSC Adv. 6(45) (2016) 39144-39149. doi: 10.1039/c6ra04444a
[32] C. Clavero, Plasmon-induced hot-electron generation at nanoparticle/metal-oxide interfaces for photovoltaic and photocatalytic devices, Nat. Photonics 8(2) (2014) 95-103. https://doi.org/10.1038/nphoton.2013.238.
[33] L. Zhu, S. B. Jo, S. Ye, K. Ullah, W. C. Oh, Rhodamine B degradation and reactive oxygen species generation by a ZnSe-graphene/TiO_2 sonocatalyst, Chinese J. Catal. 35(11) (2014) 1825-1832. https://doi.org/10.1016/S1872-2067(14)60158-3.
[34] B. Kalyanaraman, M. Hardy, R. Podsiadly, G. Cheng, J. Zielonka, Recent developments in detection of superoxide radical anion and hydrogen peroxide: opportunities, challenges, and implications in redox signaling, Arch. Biochem. Biophys. 617 (2017) 38-47. https://doi.org/10.1016/j.abb.2016.08.021.
[35] J. Marangon, H. D. Correia, C. D. Brondino, J. J. Moura, M. J. Romão, P. J. González, T. Santos-Silva, Kinetic and structural studies of aldehyde oxidoreductase from *desulfovibrio gigas* reveal a dithiolene-based chemistry for enzyme activation and inhibition by H_2O_2, PloS one 8(12) (2013) e83234. https://doi.org/10.1371/journal.pone.0083234.
[36] X. M. Zhu, C. Fang, H. Jia, Y. Huang, C. H. Cheng, C. H. Ko, Z. Chen, J. Wang, Y. X. J. Wang, Cellular uptake behaviour, photothermal therapy performance, and cytotoxicity of gold nanorods with various coatings, Nanoscale 6(19) (2014) 11462-11472. doi: 10.1039/c4nr03865g
[37] B. Bauer, D. S. Miller, G. Fricker, Compound profiling for p-glycoprotein at the blood–brain barrier using a microplate screening system, Pharm. Res. 20(8) (2003) 1170-1176. https://doi.org/10.1023/A:1025040712857.
[38] N. Engel, A. Falodun, J. Kühn, U. Kragl, P. Langer, B. Nebe, Pro-apoptotic and anti-adhesive effects of four african plant extracts on the breast cancer cell line MCF-7. BMC complement. Altern. Med. 14(1) (2014) 1-13. https://doi.org/10.1186/1472-6882-14-334.
[39] A. Gomes, E. Fernandes, J. L. Lima, Fluorescence probes used for detection of reactive oxygen species, J. Biochem. Biophys. Methods 65(2-3) (2005) 45-80. https://doi.org/10.1016/j.jbbm.2005.10.003.